

# PA vessel: Practical 3D Vessel Structure Sensing through Photoacoustic Effects with Its Applications in Palm Biometrics

ZHENGXIONG LI, YUEHANG WANG, ADITYA SINGH RATHORE, CHEN SONG, NIKHILA NYAYAPATHI, TRI VU, JUN XIA, and WENYAO XU, University at Buffalo, the State University of New York, USA

The blood vessels are the most critical part of the human circulatory system. Information acquired on the structure and status of blood vessels drives the development of numerous medical and biometric applications. Therefore, it is of paramount importance to find an effective way to sense vessel structures. Traditional methods, including infrared and Doppler sensing modalities, are limited by optical diffusion and ultrasonic scattering that are not good at vessel sensing with high performance. In comparison, we argue photoacoustic (PA) sensing is an emerging technique that can image 3D vessel structure deep in tissue with high-resolution visualization, maintaining the advantages of both optical and ultrasound methods. In this work, we propose and develop *PA vessel*, a practical 3D vessel structure sensing system based on PA effects. The entire sensing system comprises two key components, PA sensing hardware and PA sensing software. Specifically, the hardware mainly consists of a linear ultrasound transducer array, an ultrasound data acquisition system, and a neodymium-doped yttrium aluminum garnet (Nd:YAG) laser. After receiving the PA raw data, we use the advanced image reconstruction and 3D photoacoustic vein model to establish the 3D vessel structure model. We validated its effectiveness, cost-effectiveness and high resolution of *PA vessel* in the evaluation. The system achieves 52% higher signal-to-noise ratio (SNR) compared to the other methods. Furthermore, considering the 3D palm vein contains high dimensional human features and is almost impossible to forge, we also explored its applications in palm biometrics. In a pilot study with 10 participants, *PA vessel*, combined with a 3D vessel structure matching algorithm (*EMD-VT*), has proven to possess high accuracy and robustness as a biometric. *PA vessel* achieves the precision and recall of 98.33% and 97.37%, respectively.

CCS Concepts: • **Computer systems organization** → **Embedded and cyber-physical systems**; • **Security and privacy** → **Biometrics**;

Additional Key Words and Phrases: Photoacoustic Sensing; 3D Vessel Structure; Biometrics

## ACM Reference Format:

Zhengxiong Li, Yuehang Wang, Aditya Singh Rathore, Chen Song, Nikhila Nyayapathi, Tri Vu, Jun Xia, and Wenyao Xu. 2018. PA vessel: Practical 3D Vessel Structure Sensing through Photoacoustic Effects with Its Applications in Palm Biometrics. *Proc. ACM Interact. Mob. Wearable Ubiquitous Technol.* 2, 3, Article 122 (September 2018), 24 pages. <https://doi.org/10.1145/3264932>

## 1 INTRODUCTION

The blood vessels are the most critical part of the human circulatory system that transports blood and other vital factors, such as glucose and amino acids, throughout the entire body. These vessels enact a crucial role in body thermoregulation, thereby influencing daily-life activities and health conditions. Furthermore, the profound

---

Address comments to [wenyaoxu@buffalo.edu](mailto:wenyaoxu@buffalo.edu).

Authors' address: Zhengxiong Li; Yuehang Wang; Aditya Singh Rathore; Chen Song; Nikhila Nyayapathi; Tri Vu; Jun Xia; Wenyao Xu, University at Buffalo, the State University of New York, Amherst, NY, 14260, USA.

---

Permission to make digital or hard copies of all or part of this work for personal or classroom use is granted without fee provided that copies are not made or distributed for profit or commercial advantage and that copies bear this notice and the full citation on the first page. Copyrights for components of this work owned by others than ACM must be honored. Abstracting with credit is permitted. To copy otherwise, or republish, to post on servers or to redistribute to lists, requires prior specific permission and/or a fee. Request permissions from [permissions@acm.org](mailto:permissions@acm.org).

© 2018 Association for Computing Machinery.

2474-9567/2018/9-ART122 \$15.00

<https://doi.org/10.1145/3264932>

information acquired from the precise structure and status of blood vessels drives numerous applications in the medical and biometric applications. For instance, continuous monitoring of a vessel's structure present in the human foot during daily life can prevent Charcot's foot [71], which is a vascular complication frequently observed in diabetic patients and eventually leads to amputation. For secure biometric applications, accurate palm vein sensing possesses superior reliability and tamper-resistance against current recognition techniques, *i.e.*, fingerprint, hand geometry and face [9, 23, 31].

Presently, conventional vessel sensing techniques can be classified into two widely used types, ultrasound sensing (*i.e.*, Doppler) and optical sensing (*i.e.*, infrared, X-ray, thermal imaging). Doppler sensing modalities are typically employed to extract the velocity of blood flow in a variety of tissues. Extensive studies demonstrate use of color Doppler ultrasound for non-invasive sensing blood flow [79]. However, this method is insufficient for acquiring the vessel structure due to the inferior spatial resolution (Rayleigh Criterion) caused by the elongated acoustic wavelength for deep tissue penetration. Infrared sensing includes deployment of hand-vein scanners, processing the infrared images and utilizing a graph matching algorithm for dorsal vein authentication [35, 69]. Nevertheless, the deficient imaging depth of the scanners limits the overall performance of the system. Other vessel sensing techniques involve an X-ray angiographic system for vessel reconstruction [15] and thermal imaging of palm-dorsal vein patterns for personal verification [29]. However, these techniques require expensive computational devices, are sensitive to ambient temperature and suffer from low resolution. Moreover, these solutions typically provide 2D vessel information and are lacking the more robust 3D view of a vessel's structure, thereby limiting their applicability to broader healthcare systems in daily life. Therefore, a new sensing modality to enable cost-effective and precise 3D vessel monitoring is needed.

In this work, we explore a novel vessel sensing paradigm, namely photoacoustics (PA). Photoacoustics is an imaging modality that relies on listening to the 'sound' generated by the 'light', which has the advantages of both optical and ultrasound modalities. Compared to the restricted optical diffusion (less than 1mm in the skin), the photoacoustic imaging employs ultrasonic scattering coefficient in tissue which is two to three orders smaller in magnitude [74, 75]. In addition, because either unscattered or scattered photons can trigger the photoacoustic signals, photoacoustic waves currently can be generated several centimeters deep into tissue. Compared to standard techniques, PA is superior in penetration depth and high sensing resolution and contrast. Currently, PA sensing has become the research hotspot for non-invasive monitoring of a vessel's structure and it has been widely leveraged in various applications such as chemical detection [80], temperature sensing [27], and medical diagnostics [57].

To this end, we propose our system, *PAvessel*, to facilitate the 3D vessel sensing system and confirm the photoacoustic effect. We address the three main challenges in the current PA sensing paradigm: (i) a traditional PA sensing modality consumes an excessive amount of energy for generating the PA signal. To ensure that the sensing devices are practical to use over an extended period, it is crucial to address the issue of significant power consumption from the excitation source of the laser; (ii) the reconstructed model of the 3D vessel's structure through PA sensing must be of high resolution to maximize the performance of the system. However, modification of typically used transducer arrays in the conventional PA sensing setup is expensive and requires advance operational skills; (iii) to employ PA as a potential biometrics, the sensing modality must be highly accurate and robust to variation in palm poses and working environment. We first investigate a novel optimization algorithm for opportunistic sensing, which consumes less than 90% laser energy compared to the typical PA sensing system. Without extensively modifying the imaging geometry of the PA system, we achieve high resolution during sensing through utilizing an advanced image reconstruction technique and integration of the mechanical movements. To explore the performance of PA sensing as a potential biometrics, we perform comprehensive evaluations to assess the authentication accuracy and robustness of our proposed system. Specifically, *PAvessel* can achieve high resolution with 52% higher signal-to-noise ratio (SNR) with respect to the other methods and low energy consumption (close to 475mJ/pulse). *PAvessel* employs a PA sensing device to probe the laser pulse and capture

the received ultrasonic emission. To obtain an accurate 3D view of the vessel structure, *PA vessel* utilizes advanced image reconstruction and 3D photoacoustic vessel structure modules taking into consideration the limitations in the field of view (FOV) and spatial resolution. Furthermore, we perform a case study to extend the application of *PA vessel* to the biometrics domain by characterizing the features in palm vein structure and developing a vessel structure matching algorithm (*EMD-VT*) for effective and robust authentication under different real-world scenarios.

To summarize, our contribution in this work is three-fold:

- We prove the fundamental concept of the photoacoustic effect with step-by-step experimentation. We further design and implement a low-cost and efficient PA sensing system based on the vascular structure.
- We design a novel PA signal processing technique to reconstruct the 3D model of the vessel structure. We evaluate our proposed sensing system, *PA vessel*, through intensive experiments to illustrate its high throughput and resolution while being energy-efficient and cost-effective. More importantly, *PA vessel* can be immediately deployed in real-world healthcare applications.
- We investigate the unique contributor in vessel structure and employ *PA vessel* for palm vein authentication. We demonstrate the effectiveness and robustness of our proposed system under different conditions with 10 volunteers, with results indicating an exceptional authentication accuracy up to 97%.

The remainder of this paper is organized as follows: a comprehensive overview of existing work about vessel structure sensing is introduced in the related work of Section 2. Section 3 introduces the basic principles, physical mechanisms and the practical challenges of PA, as well as PA applications. Section 4 describes the PA sensing system, PA sensing architecture, hardware prototype and design considerations. In Section 5, image reconstruction and the 3D photoacoustic vessel structure model are introduced. Section 6 covers the system implementation and PA sensing system evaluation of the 3D vessel structure. A biometric application with the 3D palm vein matching algorithm and the real-world evaluation are carried out in Section 7. Section 8 offers a final discussion and we conclude our work in Section 9.

## 2 RELATED WORK

In this section, we conduct a comprehensive review of vessel sensing technologies, including two representative modalities, ultrasound and optical sensing. In addition, we also summarize the PA practical applications in other fields in Section 3.2 and discuss potential applications in healthcare and medicine in Section 8.2.

### 2.1 Ultrasound Sensing:

**Doppler sensing:** Back in 1990, Dorit D.Adler *et al.* utilized Doppler ultrasound to detect the small vessel flow [1]. In 2003, Veyrac *et al.* proposed Doppler ultrasound allows recognition of crossing vessels with high sensitivity of more than 92.8% [72]. In [79], M.C.Y.Wong *et al.* designed a high-level ultrasound Doppler scanner to visualize crossing vessels in pediatric hydronephrosis in 2017. However, as we mentioned before, these works are based on the velocity of blood flow in a variety of tissues, and the spatial resolution is limited to the tissue penetration depth. Thus, it is not adequate for vessel structure sensing.

### 2.2 Optical Sensing:

**Infrared sensing:** Other studies in this domain include the development of a low-cost hand vein scanner, an acquisition device for processing the captured images of an infrared hand and a graph matching algorithm for a dorsal vein hand verification system [20, 49]. However, we know that these solutions presented by the aforementioned studies suffer from inadequate imaging depth of their scanners, thereby limiting the performance of the system. Our PA technique, in contrast to these infrared methods, can achieve significant imaging depth

capturing more vivid detail of the microvascular structure. It is worth mentioning that while IR penetration depth is only 3.5mm at 850nm wavelength, PA is able to achieve analysis on finer granularity (1-4 cm at best).

**X-ray sensing:** The study of X-ray sensing of veins goes back to the 1990s. Noboru Niki *et al.* described a 3D image reconstruction method using an X-ray angiographic system to realize 3D imaging of blood vessels in [50]. In 2017, Cedola *et al.* presented an X-ray phase-contrast tomography to obtain a 3D characterization of encephalomyelitis lesions with imaging of the vascular structure [11]. However, this kind of technology requires a bulky and expensive rotation device and X-ray does harm to the body, which is not suitable for daily life.

**Thermal sensing:** Thermal sensing has been explored by many researchers. Im *et al.* employed a charge-coupled device (CCD) camera to capture vein-pattern images [28] in 2000. Then, Lin *et al.* proposed a novel approach using thermal images of palm-dorsal vein patterns for personal verification [41]. In 2017, Huai Geng Zheng [92] investigated the classification of hands for biometric applications through the static and dynamic analysis of near infra-red (NIR) dorsal hand vein images. However, adverse effects were observed on the performance of the system by ambient temperature, the condition of vein walls and surrounding temperature. Lin mentioned the non-triviality of these challenges and highlighted the need for combining vein patterns with other biometrics for verification.

### 3 A NEW PARADIGM OF PHOTOACOUSTIC SENSING

#### 3.1 Background

**Photoacoustic Sensing History:** Photoacoustic effect was first observed in 1880 by Alexander Graham Bell when he discovered the occurrence of sound from the absorption of modulated sunlight [8]. Prior to the development of laser in 1960, research in photoacoustics was sporadic at best [6]. With the emergence of sensing technologies, PA sensing gained momentum with a majority of the applications based on heating of the laser-induced surface, generating acoustic waves in a gas medium that was detected using a microphone. The first biomedical images using photoacoustics were obtained in the mid-1990s, though the actual breakthrough with *in vivo* imaging only began after mid-2000s. From here onwards, the field of PA has experienced rapid advancement in the instrumentation and reconstruction algorithms, functional and molecular imaging, *in vivo* clinical imaging and biomedical research. PA systems possess significant advantages as they are non-toxic and radiation-free while generating high-resolution images. One of the most notable research studies was of PA imaging in biomedicine by L. Wang [85]. The study comprehensively used several imaging techniques and reconstruction algorithms, thereby building the foundation for current PA bio-imaging. Other significant contributions in this domain include PA imaging from organelles to organs, 3D technique on blood vessels and mouse experiments, and so on [48, 76, 88].

**Photoacoustic Sensing Physical Mechanisms:** As illustrated in Figure 1, the photoacoustic effect is based on the principle of tissue excitation by light. When the tissue is stimulated with short duration pulses of electromagnetic radiation, it absorbs a portion of energy which generates heat and causes expansion. This thermoelastic expansion in tissue further generates acoustic waves. Specifically, short laser pulses of a few nanoseconds produce a wideband ultrasound signal. A typical pulsed laser generates a pulse of 10ns duration, lower than both the thermal and stress confinements [83]. The photoacoustic pressure ( $p_0$ ) that causes the acoustic waves can be defined as follows:

$$p_0(\vec{r}) = \Gamma \mu_a F(\vec{r}), \quad (1)$$

where  $\mu_a$  is the absorption coefficient and  $F(\vec{r})$  is the local optical influence.  $\Gamma$  represents the Grueneisen parameter which increases with the rise in temperature [83]. Thus, the phenomenon of the formation of sound waves following light absorption is called photoacoustic effect. PA sensing systems detect the output acoustic signal and back-propagate their data to locate the source of the signal.

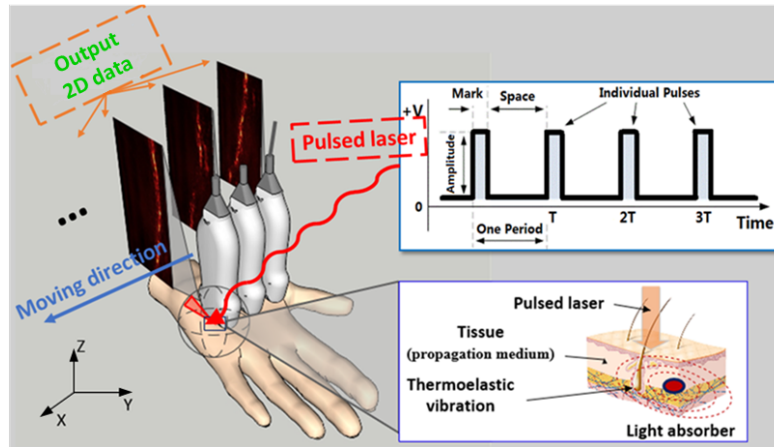


Fig. 1. Photoacoustic effect and demonstration of overall PA model. A pulsed laser is used to illuminate the tissue which generates a photoacoustic signal. To overcome the constraint of limited scan area, the transducer is automatically moved across the palm to capture the entire vein structure.

Concerning biological tissue, the ideal wavelength for minimum optical scattering with photoacoustics is close to the infrared region (600-900nm). A laser is typically used as the source of excitation [6], while the ultrasound transducers are leveraged to detect the acoustic signals. Based on the speed of sound and time of travel, we can reconstruct the image along with depth information. Due to the sparse ultrasound scattering in biological tissue, PA sensing modality is preferred over purely optical systems. In general, photoacoustics depends on two primary factors, i.e., optical absorption and scattering properties, of which optical absorption is the dominant factor. Furthermore, the PA sensing system is capable of generating images with high contrast, thereby being ideal for the visualization of microvasculature to capture distinct features in the palm vein.

### 3.2 Broader Applications of PA Sensing in Various Fields

PA sensing is arguably one of the most novel techniques that has emerged in the past decade. To date, numerous studies have been performed to advance this field, further categorized in Table 1.

**Biomedicine:** Photoacoustics has emerged as a prominent imaging modality for biomedical applications. PA sensing has brought a transformative effect across a broad spectrum, including vascular biology [10, 82], oncology [12, 66], neurology [26, 77], ophthalmology [32, 67], dermatology [19, 91], gastroenterology [58, 87], and cardiology [70, 90], while the imaging objects vary from small animals to human beings [7]. Additionally, PA sensing can also be applied to guide biopsy [34] and photothermal therapy [13]. It has drawn interest of applied physicists, applied mathematicians and clinical imaging specialists who continue to explore novel techniques for advancement of this field.

**Material Science:** A few decades ago, the concept of the photoacoustics was used for solid, liquid, and gaseous material characterization [25, 78]. In recent years, PA sensing has been successfully applied in detection of chemical gases [14, 52], flow meters [36], chemical warfare agents and explosives [52], and food inspection [16, 17, 47, 54].

**Structural Engineering:** Due to the sensitivity of the amplitude of the PA signal and its impact on an object's temperature, PA sensing can precisely monitor fluctuations in the temperature of the object. Thus, this technique has been increasingly applied to monitor temperature [53], the heating effect on micro-bubble [45] and the thermal flowmetry [44].

Table 1. List of diverse PA applications and embodiments over the years.

Areas	Year	Authors	PA applications
Biomedicine	2014	Liang C. <i>et al.</i> [13]	Photothermal Therapy
	2014	Xia J. and Wang L. [82]	Vascular biology
	2012	Paul B. <i>et al.</i> [7]	Animal or human imaging
	2012	Rowland KJ. <i>et al.</i> [58]	Gastroenterology
	2011	Favazza <i>et al.</i> [19]	Dermatology
	2010	Taruttis A. <i>et al.</i> [70]	Cardiology
	2010	Staley J. [66]	Oncology
	2010	Jiao SL. <i>et al.</i> [32]	Ophthalmology
	2010	Kim C. <i>et al.</i> [34]	Guide Biopsy
	2009	Hu S. <i>et al.</i> [26]	Neurology
Material Detection	2018	Deepa <i>et al.</i> [22]	Chemical Gas Detection
	2018	Mikael <i>et al.</i> [36]	Flow meter
	2016	Tauhidur <i>et al.</i> [54]	Food inspection
	2008	CKN Patel [52]	Chemical warfare agent and explosives
Temperature Sensing	2018	Lum <i>et al.</i> [45]	Temperature effect on microbubble
	2017	Liu Wei <i>et al.</i> [44]	Thermal flowmetry
	2009	Pramanik <i>et al.</i> [53]	Vivo temperature monitoring

### 3.3 Practical Challenges

Presently, the majority of the PA techniques can be only applied in a controlled lab environment. To broaden the scope of PA sensing in real-world applications, it is crucial to address the following challenges:

- (1) **Energy-Efficiency:** The PA sensing system requires excessive energy for generating the PA signal. The power consumption mainly originates from the excitation source to produce a continuous laser. We replace the scanning approach with the opportunistic optimization sensing, which consumes less than 10% of the laser energy. To solve the problem of discontinuous vein segment resulting from the intermittent sensing, we develop comprehensive algorithms to establish the 3D vessel model [86].
- (2) **High-Throughput:** Conventionally, the PA sensing time/delay is immensely constrained by the FOV on the probe. To enlarge the imaging FOV, we substitute the single circular optical fiber bundle with a bifurcated line fiber bundle. Moreover, the data acquisition system is updated to double the imaging speed. Instead of linear transducer arrays, we leverage the ultrasound transducer array to eliminate the need for translational scanning for accelerating the imaging speed.
- (3) **Low-Cost:** For a general 3D PA sensing system, a considerable amount of cost arises from multiple transducers and their deployment. In this work, we achieve a steady and robust 3D vein sensing by employing a novel PA architecture utilizing single transducer arrays and the motor platform.
- (4) **High-Resolution:** The commercially available single transducer arrays are low-cost, convenient and are widely clinically recognized. However, resolution is severely limited. We address this limitation by developing an extensive image reconstruction technique with the integration of mechanical movement, by ensuring no modification to the imaging geometry and the concerned system.

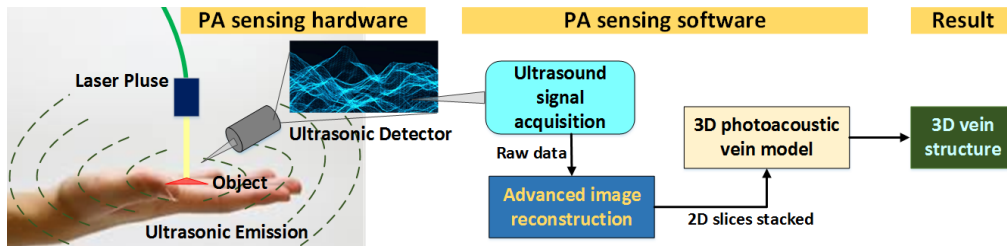


Fig. 2. The system overview of a cost-effective vein sensing system via photoacoustic effects.

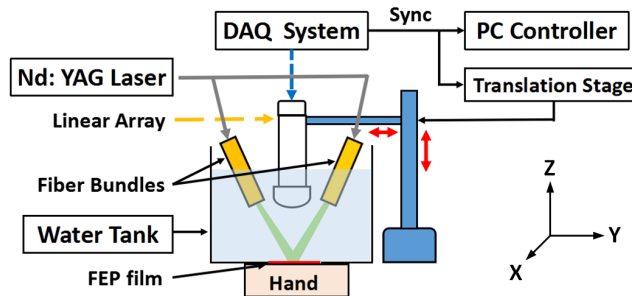


Fig. 3. The setup of the PA sensing module, which includes a linear array transducer, a fiber bundle, a laser source, a container, a translation stage and a trigger system.

## 4 PHOTOACOUSTIC SENSING ARCHITECTURE OVERVIEW

### 4.1 *PA vessel* Overview

We describe our proposed system, *PA vessel*, during a real sensing routine in Figure 2. The entire system involves combined efforts from the **hardware** and the **software** modules. (i) First, the **hardware** module: hand is placed under the laser, emitting a multi-dimensional ultrasound wave pattern due to the photoacoustic effect. Because acquiring the precise pattern in the analog domain is not feasible, we perform dimension reduction to lower the field measuring complexity while keeping the salient information for the vein structure. Specifically, we select a Region of Interest (ROI) on the palm to reduce the signal dimension from analog to digital domain, to further ensure that the PA sensing is ‘computational’. Besides integrating the original complex field into low-dimensional digital representation, it also guarantees a low sensing delay by the bifurcated line fiber bundle and the ultrasound transducer. We elaborate on our novel hardware design for PA sensing in Section 4.2. (ii) Then, the **software** module: the data format obtained from the PA sensing is a time series signal for which a leading image reconstruction technique is utilized to guarantee the preservation of information. Our 3D PA vein model employs a comprehensive series of parameters for tracking and connecting functions to store the vein structure from multiple slices of 2D data while achieving memory and runtime simplicity.

### 4.2 The Sensing Architecture and Hardware Design

In this section, we describe our optimized PA sensing system whose schematic is shown in Figure 3. The system comprises seven primary components, including an excitation source, linear array, fiber bundles, DAQ system, PC controller, translation stage and water tank. First, the excitation source emits a laser through the fiber bundles and water tank onto the hand. The translation stage moves the laser scanning point across the ROI. Subsequently, the linear transducer array captures the emitted ultrasound signal and converts it to the DAQ system. The PC governs the entire process and finally computes the received signal from the DAQ system.

**4.2.1 Hardware Design: PA Signal Parameters Consideration.** During the hardware design, it is necessary to consider the following PA signal parameters:

**Ultrasound Wavelength:** As discussed in Section 3.1, we require short duration laser pulses to achieve the pressure necessary for generating a wideband ultrasound signal. In general, a pulsed laser has a 10ns duration. The wavelength is chosen based on the absorption coefficient of the endogenous tissue chromophores or the optical absorbers. These chromophores are typically hemoglobin, melanin and water [83]. To precisely image the vessel vasculature, we customize our wavelength based on the optical absorption of hemoglobin. At 1064nm, we observe a sufficient optical absorption and penetration depth.

**Propagation Medium:** The propagation medium for ultrasound must be similar to the tissue suffering from the thermoelastic vibration. Consequently, it is vital that the environment of the transducer and fiber outputs are closely akin to the vessel environment.

**Laser Intensity:** It is a known fact that the safety range of the laser beam intensity on the skin surface is less than  $100\text{mJ}/\text{cm}^2$  [84]. Thus, careful consideration must be given in selecting a laser to ensure it is strong enough to penetrate the skin tissue, while meeting the safety requirement.

**4.2.2 Hardware Prototype.** To maximize the system efficiency, a careful selection of hardware is necessary for *PA vessel*. Several constrains are summarized for the hardware selection: (i) a high power laser with 1064 nm output to provide deep penetration depth; (ii) a fiber bundle to deliver the light onto the hand; (iii) a linear transducer array with sufficient FOV and spatial resolution; (iv) a high gain ultrasound data acquisition system (DAQ) to provide adequate SNR; (v) a translation stage with long stroke to cover the center of the human palm; (vi) a PC to control translation stage movement, data acquisition and light illumination; (vii) a water tank to use as the propagation medium. To realize this, our hardware design incorporates the following:

**Excitation Source:** A 10-ns-pulsed Nd:YAG laser is chosen in our design. It has a 10Hz pulse repetition rate and 1064 nm output wavelength (Continuum, SLIII) and leverages a crystal as a laser medium for solid-state lasers. It is optically pumped using a flashtube or laser diodes. Furthermore, it is the most widely used type of laser [64] and is capable of functioning on almost all skin types, including tanned or darker skin tones, with high pulse energy.

**Fiber Bundles:** Considering that light can only be observed from the side of the linear transducer array, a bifurcated fiber bundle can offer a superior uniform illumination than single fiber bundle. Therefore, we design a specialized mount through 3D printing to make the bifurcated fiber bundle, capable of providing high resolution. It comprises of 1.1-cm-diameter circular input and two 5.1-cm-length line outputs (Schott Fostec).

**Linear Transducer Array:** For the linear transducer array, we prefer a 3.8cm wide transducer array with 5MHz central frequency and 128 elements (ATL L7-4). The L7-4 probe works in 4.0-7.0MHz, which can be utilized for vascular and small parts applications. It supports a high lateral resolution and adequate FOV. During the experiments, the ultrasound transmit function of the L7-4 transducer array is disabled and the transducer array only receives PA signals. This can be achieved by modifying the setting of the research ultrasound system through Matlab.

**DAQ System:** In the DAQ system, the gain is a significant factor as a higher gain results in an efficient system with higher SNR. We leverage a 54dB gain research ultrasound DAQ system (Vantage 128, Verasonics), which is the maximum gain that can be enabled for PA data acquisition among all other accessible research ultrasound DAQ system. In addition, the Vantage platform from Verasonics is the only commercially available system with the flexibility to enable a broad scope of ultrasound research. It is capable of performing the digital averaging, filtering and decimation up to 1000 acquisitions to improve the SNR and reduce bandwidth.

**Translation Stage:** For better subject positioning, a 10cm stroke translation stage (McMaster-Carr) is applied, which is sufficient to cover the ROI and convenient to attach a stepper motor. The linear array is mounted on a horizontal XY plane, while the laser head is translated in the vertical Z direction.

**PC Controller:** We adopt the Dell Precision T5610 for the host controller. Its working environment is Windows 7 64-bit with 2× Intel Quad Core Xeon and Intel 180GB SSD. The PA sensing software works on the Matlab. For controlling the system, the synchronization of all components is achieved by using the trigger output of the laser to prompt the motor movement and data acquisition process. An I/O device (PCI-6115, National Instruments) is installed on the PC controller to receive the trigger and control the stepper motor.

**Water Tank:** It is a known fact that the vessel contains more than 90% water. Thus, for the propagation medium, we built a personalized water tank and kept the bottom as open. Subsequently, the transducer and optical fiber outputs are submerged into the tank. The bottom of the water tank is sealed with 0.05mm thickness fluorinated ethylene propylene (FEP) plastic film (McMaster-Carr) to allow the imaging of the object through this window. The film is optically and acoustically transparent.

## 5 PA SENSING SIGNAL PROCESSING SCHEME

In this section, we introduce our 3D PA vein model. The entire process can be categorized in two phases. During the first phase, we develop a preprocessing algorithm to obtain the vascular structure from the PA image. Other unrelated information, such as tissue, muscle and skin characteristics are excluded from the PA image. In the second phase, after acquiring the vascular structure, we extract the fiducial points to represent the biometric features in individual vein structure. Feature extraction has the potential to enhance the robustness and efficiency of the vein model establishment. In other words, we construct the topology of the vein and form the vascular structure as the feature set. The overview of our model is illustrated in Figure 4, comprising four primary steps based on their functionalities, *i.e.*, advanced image reconstruction, 3D vein synthesis, 3D vein segmentation and 3D vein structure reconstruction. Considering our work is the first exploratory paper, we use the palm vein for better understanding. Furthermore, the palm vein possesses the following characteristics: (i) it is widely used and easily accessible in daily life; (ii) it contains a rich set of unique geometric features in different granularity levels which are essential to examine the performance of our system.

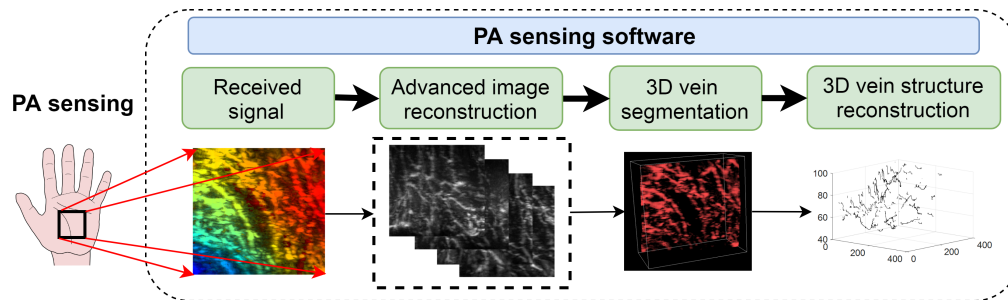


Fig. 4. *PA vessel* software scheme illustration.

### 5.1 Advanced Image Reconstruction

Following the data acquisition for PA, we perform image reconstruction for subsequent data analysis. In our work, an explicit 3D reconstruction is not executed since it is highly susceptible to hand movement and requires an extensive reconstruction period. Given that we can solely scan the palm along one direction, the universal back-projection algorithm [84] is applied for PA image reconstruction. As described in section 3.1, the initial PA pressure at position  $r$  excited by the  $\delta(t)$  EM pulse equals  $p_0(r) = \Gamma(r)A(r)$ , where  $A(r)$  is the spatial EM absorption function and  $\Gamma(r)$  is the Gruneisen parameter. Based on the mentioned literature [84], when an ultrasonic detector at position  $r_0$  receives PA signals emitted from source  $p_0(r')$ , the equation can be expressed in the back-projection

form as follows:

$$p_0^b(r') = \int_{\Omega_0} b(r_0, \bar{t} = |r' - r_0|) \frac{d\Omega_0}{\Omega_0}, \quad (2)$$

where  $b(r_0, t) = 2p(r_0, t) - 2t \frac{\partial p(r_0, t)}{\partial t}$  at position  $r_0$  and  $\frac{d\Omega_0}{\Omega_0}$  is a factor weighting the contribution to the reconstruction from the detection element. The reconstruction simply projects the quantity  $b(r_0, t)$  backward on a spherical surface related to position  $r_0$ . Predominantly, for every element of the detector, the pressure waveforms recorded are back-propagated to each corresponding radius calculated from the traveling time of sound. The sum of the entire set of signals from these elements to one pixel constructs its final intensity. We use Matlab to reconstruct each 2D slice, after which all 2D slices are stacked relative to the scanning direction, thereby forming a 3D image of the palm vasculature.

## 5.2 3D Photoacoustic Vein Model

**5.2.1 3D Vein Segmentation.** In this section, we describe the approach to 3D Vein Pattern Segmentation. This step is critical in order to achieve better performance in our system. We develop a preprocessing algorithm to obtain the blood vessels from the PA image. Other unrelated information, such as tissue, muscle and skin related will be removed from the 3D sensing imaging.

In segmentation, volume rendering is an essential primary step to find the blood flow against the ground area. The original acquired sensing data includes noises caused by the imperfection of the sensor array or the environmental noise in the propagation medium. To eliminate these noises, a Gaussian blur filter is applied. The reason is that these noises are high frequency and Gaussian blur is a low-pass filter. Furthermore, employing a Gaussian blur to an image is identical to using a Gaussian function for convolution of image [37, 73]. It attenuates high-frequency noises in the acquired sensing data. Next, without detecting the rough blood flow first as other principal methods, the blood flow is extracted by the image binarization. There are many existing methods in Computed Tomography (CT) or Magnetic Resonance Imaging (MRI) sensing to extract the blood flow from the background [21, 89]. They detect the blood flow edge or centerline to locate the blood flow area first and then obtain the segmented vessel tree using binary-based, filter-based or cluster-based approaches. With these sensing technologies, the blood flow in the image is not distinctive, owing to low imaging resolution, light scattering in the skin layer and optical blurring. Therefore, blood flow must be located at the start. However, PA sensing imaging has several accepted advantages in that the resolution of the sensing image is extremely high and there is no light scatter or optical blurring. The blood flow in the PA image is outstanding. Therefore, we could directly determine the blood flow from the background area employing the image binarization to reduce the processing time, without impacting system performance. Succeeding the analysis of histograms of the gathered images, we define the global threshold for binarization. This preprocessing approach is computationally very lightweight.

**5.2.2 3D Vein Structure Reconstruction.** In this section, we first establish the vein structure and then extract features based on the analytical geometry and optimization techniques. Then, we obtain the fiducial points to portray biometric features in each palm. We construct the topology of the hand vein and form the vascular structure as the feature set.

To gain the vascular structure, it is significant to primarily track each blood flow as a vessel among the successive image slices. It is because we find the blood flow data obtained are not connected and insufficient to describe the topology of the hand vein. To repair the possible broken blood flow and form the vascular structure for later feature matching, in our work, we deploy Nearest Neighbour Search to form the vessel. The Nearest Neighbour Search is to find and link the next blood flow point in a given set that is the most identical to another blood flow point, keeping track of the "best so far" [3, 46]. Subsequently, the biometric features are discovered. After getting the vessel, we obtain a highly rough vessel set. There is still considerable redundancy in vein topology, making it difficult to find the features. Thus, we continue to connect vessels and form the vascular

	Approach			
	<i>Probability-based</i> [93]	<i>Multiscale</i> [62]	<i>Region growing</i> [2]	<b>Skeleton-based</b> [68]
Complexity of algorithm	High	Medium	High	<b>Lowest</b>
Rotation Invariance	Not inherent	Inherent like SIFT	Not inherent	<b>Inherent if graphs used</b>
Accuracy	Medium	Depends on images	Accurate	<b>Accurate</b>
Min. images	1	3	1	<b>1</b>

structure as the feature set. To refine the vessel and extract features, we employ the skeleton-based marching cubes method [68] in Algorithm 1. The points of extracted vessels, having the smallest distance, are classified depending on the amount of neighbouring background points. Afterwards, the points are removed in descending order of neighbouring background points. Lastly, a post-processing technique is leveraged to discard the vessel bifurcations, which are apparent false positives, based on their proximity to an end-point. In contrast with the other vascular structure reconstructions [2, 50, 51, 63, 93] shown in Table 2, this method is easily deployable and invariant to a rotation, as well as possess lowest lightweight computation and exceptional accuracy. The necessity of a rotation invariant algorithm is fulfilled by the vascular feature matching algorithm, proposed in the following section. Upon a careful inspection of the refined vascular structure, we identify two fundamental features in the vascular structure, zigzag and bifurcation, and are matched with the vessel theory. Specifically, zigzag is the vessel shape distribution, which is useful for the vessel to store more blood and bifurcation is where the vessel diverges to form capillaries [61]. Furthermore, if a data slice is  $n$  by  $n$  pixel size and  $m$  slices are stacked, then the capacity of the 3D PA vein model is  $2^{mn^2}$ . When  $n = 400$  and  $m = 20$ , the capacity is much large than  $10^{18}$ .

---

#### Algorithm 1 3D Vessel Reconstruction Method

---

**Input:**  $I(k)$ : Voxels  $(i,j,k)$  and the background area  $Q$

**Output:**  $V$ : The vein structure

- 1: Define the distance  $l_{ijk} = \{(i-x)^2 + (j-y)^2 + (k-z)^2 | (x,y,z) \in Q\}$ ; ▷ Define the distance
  - 2: Categorize voxels of extracted vessels having the smallest distance  $l_{ijk}$  based on the number of neighboring background voxels.
  - 3: Check each class and delete voxels of the category whose number of neighboring background voxels is the highest. ▷ Erasing voxels in descending order of the number of neighboring background voxels
  - 4: Repeat the first three steps until detecting bifurcations and end points.
  - 5: Form the skeleton based bifurcations and end points and reconstruct the vein structure  $V$ .
  - 6: **return**  $V$
- 

## 6 PA SYSTEM IMPLEMENTATION AND EVALUATION

### 6.1 System Implementation

The implementation of the whole system mainly consists of seven parts, including a PC controller, an excitation source and driver, a bifurcated fiber bundle and signal conditioning, a transducer array, a signal receiver array, a subject positioning part and a water tank. As shown in Figure 5, the palm is positioned under the water tank with an ultrasound gel applied for acoustic coupling. The fiber bundle is aligned with the laser output in order to

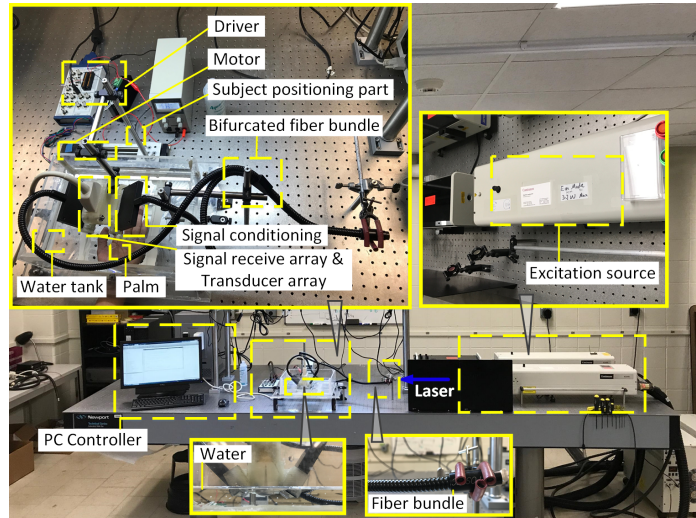


Fig. 5. *PA*vessel system integration, including PC controller, the excitation source and the driver, the bifurcated fiber bundle and the signal conditioning, the transducer array, the signal receiver array, the subject positioning part and the water tank.

deliver the light to the palm. The L7-4 transducer acquires the photoacoustic signal generated. The micro-step driver is used to control the motor speed and it moves at a step size of 0.2mm to scan the ROI.

## 6.2 Experimental Setup

All experiments are conducted according to host institutional review board (IRB) protocol.

**Participants:** 10 volunteers are recruited (5 males and 5 females). Their age ranges from 19-42, all above the age of consent (above 18 years). Although the laser part in the system implementation is within the safe range, we still follow the safety rules and require the participants to wear glasses during the experiment.

**Experimental Procedure:** For each subject, we move the transducer over a distance of 40 mm to scan an area of 38 mm (lateral length of the transducer) by 40 mm. Considering the sensing width for the transducer is 0.275mm, we set the step size 0.2mm. One sensing takes 20 seconds. During the experiment, they sit before the device as shown in Figure 6. First, they put the left palm on the specific area right below the laser fixed for 20s. Then they switch hands, keeping the right palm at the same position for 20s. Each participant repeats these two steps 10 times.

**Data Collection:** The acoustic signal is received by the Verasonics Vantage data acquisition system through the Philips L7-4 transducer array. The vascular image is reconstructed from raw data using advanced image reconstruction. Next, on the basis of the scanning direction, all 2D reconstructed images are stacked to generate a 3D image of palm vessel structure (see Section 5). For each participant, we gather one 3D palm vein structure for one time. In total, 200 3D palm vein structures are collected.

## 6.3 Comparison of PA and Infrared Vessel Sensing System

To better illustrate the PA sensing system performance, we hope to compare it to the other vessel sensing system. Infrared optical imaging is a sophisticated and widely used technique for palm vein visualization. Therefore, we perform a comparison between the acquired infrared vein images and our PA results. The infrared vein visualization system (see Figure 7(a)) consists of an infrared LED (Vastfire, IR-A100, 850nm), a CCD camera (Basler sca1390-17gm GigE), an infrared filter (Neever IR760 52mm), and two optical linear polarizers (Thorlabs, LPNIRE200-B). The infrared filter effectively removes the ambient visible light. In addition, the orthogonal setup

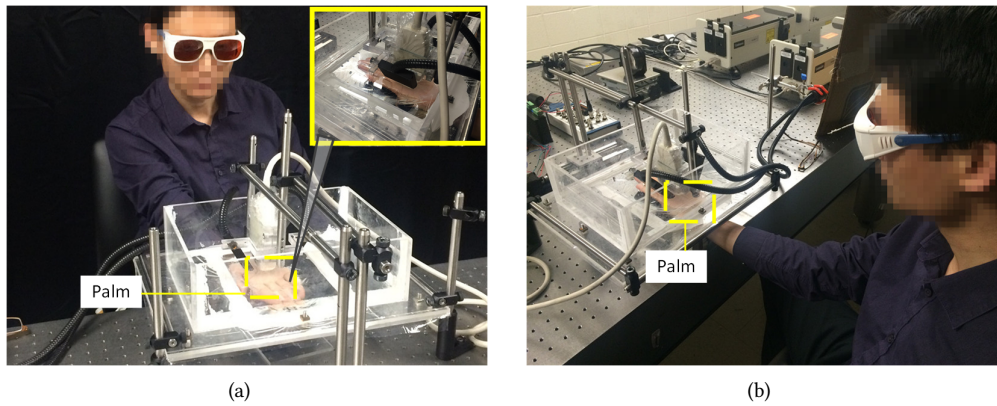


Fig. 6. (a) records the scanning procedure from front view. (b) records the scanning procedure from side view.

of two polarizers, *i.e.*, one in front of the laser and the other in front of the camera, filters out the light reflection from the skin. The light intensity on the skin surface is approximately  $12\text{mW}/\text{cm}^2$ , highly inferior to the maximum permissible exposure intensity limit of  $400\text{mW}/\text{cm}^2$ . As shown in Figure 7(b) and (c), an area of  $3.8\text{cm} \times 4\text{cm}$  (yellow box) is imaged by both PA and IR systems. The depth-encoded maximum intensity projection (MIP) PA image, illustrated in Figure 7(c), can precisely affirm the rich vascular structures, indicating the potential of PA technique to effectively determine the features distributed over 15mm in depth. The IR image is shown in Figure 7(b), with a yellow box marking the same region of PA. We observe that the blood vessels, within the yellow box, are significantly blurry. The resolutions we calculate are 1.3mm and 2mm and the SNR are 93 and 61 for PA and IR results, respectively. The PA resolution agrees with the theoretical estimation of 1.5mm along the z axis. In terms of the vessel density, for the same ROI, it can be clearly seen from Figure 7(b) and (c) that PA vascular structures are denser than those in the IR image. Additionally, PA successfully addresses the constraints of IR which is only capable of providing a 2D image having no depth information about the vasculature. To summarize, PA has a better performance than IR, from aspects of the resolution, SNR and penetration depth.

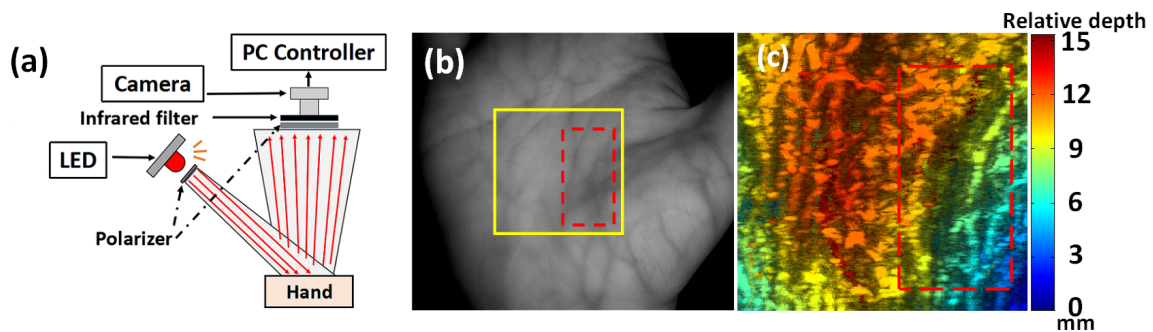


Fig. 7. The comparison between PA and IR palm vessel imaging techniques. (a) The setup of the NIR sensing system. (b) IR image of the healthy volunteer's palm. (c) Depth-encoded vascular image of the same palm. The ROI are marked in the yellow box. Red dashed boxes highlight the same vessel branch area in (b) and (c).

#### 6.4 Excitation Source Power Effect

The laser power is a crucial factor in PA sensing. To validate whether the laser power affects the PA results, we image the same palm with three different powers: 800, 650 and 475 mJ/pulse. Since the coupling efficiency of the

fiber bundle is around 60%, and the size of the laser beam on the object's surface is approximately  $2.5\text{cm} \times 6.0\text{cm}$  ( $15\text{ cm}^2$ ). The final light intensity on the skin surface is  $32$ ,  $26$  and  $19\text{mJ}/\text{cm}^2$ , which are all much less than the safety limit of  $100\text{mJ}/\text{cm}^2$  at  $1064\text{ nm}$ . As shown in Figure 8, under the same colorbar, the vessel features dim as the laser power decrease. We use the mean of vessel signal and standard deviation to calculate the SNR of these three images, and the yield SNR are  $67.36$ ,  $11.81$  and  $6.59$  for (a), (b) and (c) respectively. This result shows that higher excitation power provides the PA sensing system a stronger SNR. It is also worth mentioning that even when the laser energy reaches  $475\text{mJ}/\text{pulse}$ , nearly half of the default laser power, we can still observe the visible vessel structure, which holds the potential for the future vein sensing applications with low power consumption.

It is a known fact that the shapes of the vascular patterns of different individuals are distinctive, very stable over a long period of time and not easily stolen under the skin [30]. Due to these accepted advantages, in the following section, we continue exploring a real-world study for biometric applications based on PA vein structure sensing.

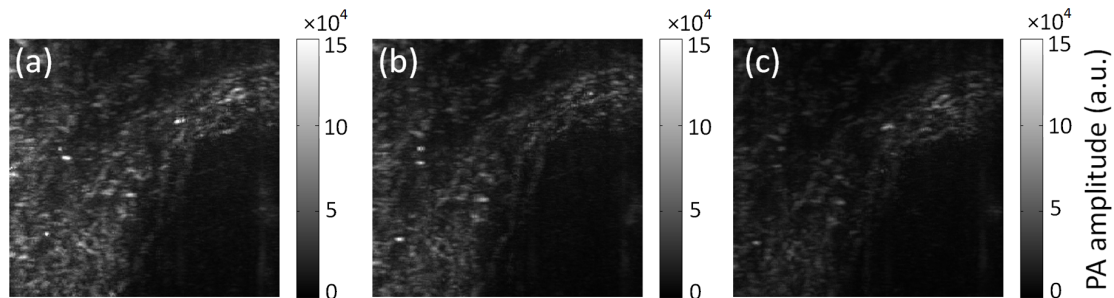


Fig. 8. Comparison of different excitation powers. (a) PA result acquired with  $800\text{mJ}/\text{pulse}$  laser power. (b) PA result acquired with  $650\text{mJ}/\text{pulse}$  laser power. (c) PA result acquired with  $475\text{mJ}/\text{pulse}$  laser power. These three images are plotted using the same colorbar.

## 7 A CASE STUDY TO PALM VEIN BIOMETRICS

### 7.1 Background and Motivation

Currently, biometrics based on the 2D images are prone to the image/model presentation attack especially when the 2D vein graph can be easily spoofed (e.g., medical records). The 3D palm vein naturally contains high dimensional human features, and more importantly, is almost impossible to forge. Thus, in this real-world study, we conduct the biometrics application based on the 3D vessel sensing.

### 7.2 Matching Methods for Biometric Applications (*EMD-VT*)

In this section, we introduce the proposed matching algorithm in the biometric system to overcome the variance from the hand rotation and hand statuses and achieve a better authentication result. Once the vascular structure as the feature set from the input is built, we compare the input with the genuine template in the database to verify its legitimacy. The vascular structure matching is based on the comparison of biometric features. The similarity among vascular structures is directly related to the similarity among biometric features. Presently, Euclidean, Hamming and Hausdorff distance are widely applied in metrics matching. In biometric, Euclidean distance is used with hand geometry [61], Hamming distance is applied for fingerprint-iris research [5] and Hausdorff distance could be found in palm print detection [40]. However, Euclidean and Hamming distance are applied in 1-to-1 matching and Hausdorff distance is used in 1-to-N matching. It needs to note that the palm vein could have a significantly larger deformation due to its physical characteristics [33]. It is not uncommon for

Table 3. The factors definition in *EMD-VT*.

Variables	Definition
A cluster	A single point in $\mathbb{R}^d$
A signature	A set of clusters
The weight of a cluster	The fraction of the vessel distribution in the cluster
A feature	One cluster
The ground distance	The distance between two features
Matching points	A pair of features with the least distance

two compared vein feature sets to have different sizes. Matching is M-to-N as shown in Figure 9. Thus, in this situation, these previous approaches could not work.

For vascular feature matching, we face two main challenges. First, in palm sensing, the results are not constant over time and the feature numbers are varied. There are many reasons, including the result from the hand position, hand status, human metabolism or muscle activity during sensing. It leads to the M-to-N matching problem, which could not be solved by Euclidean, Hamming or Hausdorff distance. Besides, the vascular structure variation in different palm poses and different palm statuses is also the other challenge.

**7.2.1 Definition.** We propose the vascular structure in terms of the clusters. Each cluster is a single point of  $\mathbb{R}^d$  and the fraction of distribution existing in the corresponding cluster determines its weight. A set of clusters is called the *signature* where every individual *signature* can have different sizes and one cluster can be thought of as a single feature in a signature. The ground distance is referred to as the distance between two features where the shorter the ground distance, the more similar are the features. The pair of features with the least distance is considered as the matching points. The definition of variables is listed in Table 3.

**7.2.2 Formulation.** Given two vascular *signature*  $A$  and  $B$  in  $\mathbb{R}^d$ , *signature*  $A$  is the tested input one and *signature*  $B$  is the genuine one template. Assume *signature*  $A$  is constituted by  $m$  clusters. *Signature*  $A$  is marked as *signature*  $A = \{(p_1, w_{p_1}) \dots (p_m, w_{p_m})\}$ ,  $1 \leq i \leq m$ , where  $p_i$  is the cluster representative and  $w_{p_i}$  is the weight of the cluster. Also, it is the same that *signature*  $B = \{(q_1, w_{q_1}) \dots (q_n, w_{q_n})\}$ ,  $1 \leq i \leq n$ . Then, let  $D = [d_{ij}]$  be the ground distance between clusters  $p_i$  and  $q_j$  with  $d_{ij} = \|p_i - q_j\|$ . In the *EMD-VT* model, the transformed cluster  $q'_i$  is satisfied with  $q'_i = Mq_i + C$ , where  $M$  is the rotation matrix and  $C$  is the translation matrix. Concurrently,  $d'_{ij}$  is bounded less than  $\delta$ , with  $d'_{ij} = \|p_i - q'_j\| < \delta$ . It is worth to mention that our objective is to find the min directional distance between two features. The directional distance is defined as flow  $F = [f_{ij}]$ , where  $f_{ij}$  is the flow, *i.e.*, corresponding (or alignment) information, between  $p_i$  and  $q'_j$ .

$$\begin{aligned}
\text{Min } & \text{EMD} - \text{VT}(A, B, F) = \frac{\sum_{i=1}^m \sum_{j=1}^n f_{ij} d'_{ij}}{\sum_{i=1}^m \sum_{j=1}^n f_{ij}} \\
\text{s.t. } & f_{ij} \geq 0, 1 \leq i \leq m, 1 \leq j \leq n \\
& \sum_{j=1}^n f_{ij} \leq w_{x_i}; 1 \leq i \leq m \\
& \sum_{i=1}^m f_{ij} \leq w_{y_j}; 1 \leq j \leq n \\
& \sum_{i=1}^m \sum_{j=1}^n f_{ij} = \min(\sum_{i=1}^m w_{x_i}, \sum_{j=1}^n w_{y_j})
\end{aligned} \tag{3}$$

These are the constraints: (i) move points from *signature*  $A$  to *signature*  $B$ ; (ii) confine the amount of points in the target that can be sent to the associated weights from the clusters in *signature*  $A$ ; 3) restrict the clusters in *signature*  $B$  from receiving points more than their capacity; 4) move the maximum amount of points.

Our problem formulation for authentication involves matching between two vascular structures, possibly having unequal length, deformation and rotation. We adopt the Earth Mover's Distance, a measure of the distance between two probability distributions over a region [59], for vascular structure matching because of three reasons: (i) the hand vein topology is essentially the movement of the corresponding points on the image, which satisfies the principle of EMD; (ii) N-to-M EMD matching can be adaptive to the variation in feature number. (iii) EMD could be extended to have a better deformation tolerance in matching, compared to other distance metrics [55, 56, 65]. Thus, we propose an extended Earth Mover's Distance for Vein Structure, namely *EMD-VT*, by enhancing two particular aspects. First, the geometric deformation is limited to a certain space due to human physical characteristics. We assume the boundary distance is  $\delta$  and no matching pair distance is larger than  $\delta$ . It is because palm vein physical characteristics stay constant throughout one's lifetime [4] and the palm vessel diameters expand among 0.5-0.9mm [38]. Therefore, geometric deformation is considered as limited to a certain range because human physical constraints and matching points are within the distance boundary. Second, according to the user habits, the pose could not be standard every time and there are variances during sensing. The pose rotation invariance is considered and the algorithm is proposed in Equation 3.

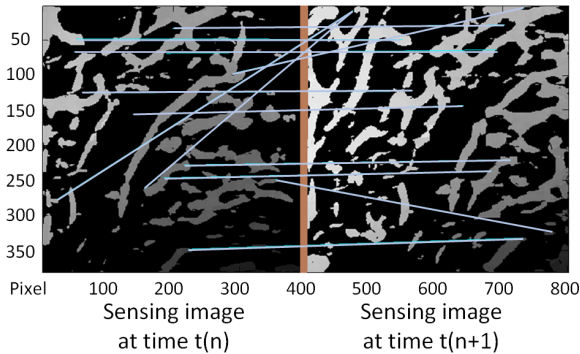


Fig. 9. M to N mapping challenge in vascular feature matching.

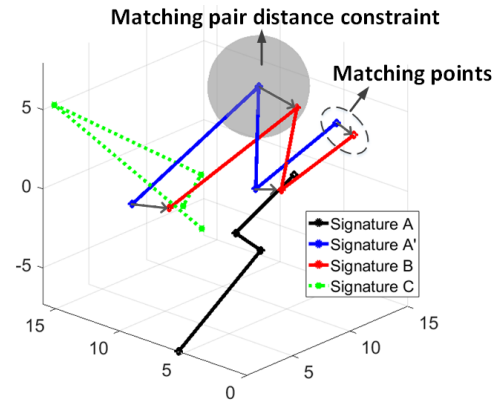


Fig. 10. *EMD-VT* matching illustration for two basic patterns.

In practice, we compare all features against the corresponding template features. For illustration, Figure 10 shows a matching result of two feature sets in vascular vein structures. In palm vein structure, zigzag and bifurcation are the fundamental features. As shown, from the geometric aspect, *signature A* and *B* are zigzag, while *signature C* is similar to bifurcated-based, implying *signature A* is matched with *signature B* and is quite different from *signature C*. Under the *EMD-VT* metric, *signature A* first rotates with a proper angle into *signature A'* and then matches with *signature B* at each point. After normalization, *EMD-VT* distance between *signature A* and *signature C* is 3 times than the value between *signature A* and *signature B*, which is matched with our analysis. However, under Euclidean, Hamming and Hausdorff distance, the distance between *signature A* and *signature C* is equal or even less than the distance between *signature A* and *signature B*. It is considered that *signature A* is closer to *signature C* than *signature B*. This is an erroneous judgment. Therefore, we select *EMD-VT* in this application.

**7.2.3 Risk Statistic.** After we compare the test input with the template, a measurement result is calculated for the user. The user will be regarded as the genuine one, when his matching result is less than a pre-defined threshold. However, sensing might contain variations, like improper hand pose. Thus, for practical purposes, we continue using risk statistics to improve the final decision [39]. First, we set the threshold as  $T$ . When the matching result

is less than  $0.7T$ , the system would immediately pass this try. However, when the result is more than  $0.7T$  and less than  $1.3T$ , the system would ask the user to tap the sense plane with full flat palm (seen in Section 6) and sense it again, which increases the signal coupling and improves the sensing result. When the second matching result is less than  $T$ , the user would be validated. Under other situations, the action fails.

### 7.3 Evaluation on PAVessel Biometrics

In this section, we integrate the PAVessel system and conduct the following evaluation experiments in the following sections. To evaluate the overall performance, we assess the correlation between the test palm veins and the corresponding template. For the robustness and usability test, we evaluate the PA setup parameter and employ volunteers scanning their hands with different hand poses. Similarly, after these, we test palm veins to verify if the system works under all environment situations.

**7.3.1 Data Partition.** For the data collection (see Section 6.2), there are 20 3D palm vein structure classes. For each 3D palm vein structure, we randomly select 5 out of 10 vein structures as the template set, and use the rest for testing. In total, 100 vein structures are used as templates and 100 vein structures are used as samples. For each sample, we compare it with each template using *EMD-VT*. We determine that the sample to be the specific template’s class is the one with the minimum average distance. If multiple classes meet the criteria, we employ the majority voting strategy to determine the class.

**7.3.2 Metrics.** In our experiments, we use the false acceptance rate (FAR), false rejection rate (FRR) and equal error rate (ERR) as evaluating metric in the overall performance analysis. FAR measures the likelihood of false acceptance of an attempt executed by an unauthorized user to access the biometric system. FRR measures the likelihood of incorrect rejection of an access attempt by an authorized user. The proportion of false acceptances equivalent to the proportion of false rejections is indicated by the EER. The lower the EER is, the better the system’s performance, as the total error rate, *i.e.*, sum of the FAR and the FRR, at the point that the EER decreases. Besides, it is natural to employ *Accuracy*, *Precision* and *Recall* for authentication system metrics [42, 43].

### 7.4 Biometric Performance Analysis

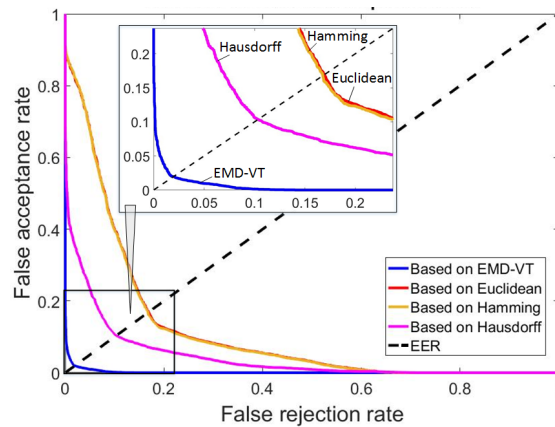


Fig. 11. Overall performance accuracy analysis.

**7.4.1 Accuracy Analysis.** For the overall performance analysis, the data are taken from the Data Partition we built using our acquisition system. We repeat the experiment 10 times and calculate their average overall performance.

In addition, in order to evaluate the *EMD-VT* matching algorithm, we compare our system against a system using other matching algorithms. The results, in terms of FAR, FRR and EER, are presented in Figure 11.

As shown in Figure 11, the EER of the whole system based on *EMD-VT* achieved is 1.93% and its accuracy is up to 97.86%. It implies that this method is feasible and more importantly, effective, for palm vein recognition while achieving exceptional accuracy. The EER of other matching algorithms are all more than 10% and their accuracy is all lower than 90%. This result shows our system has a better performance due to overcoming the N-to-M matching problem.

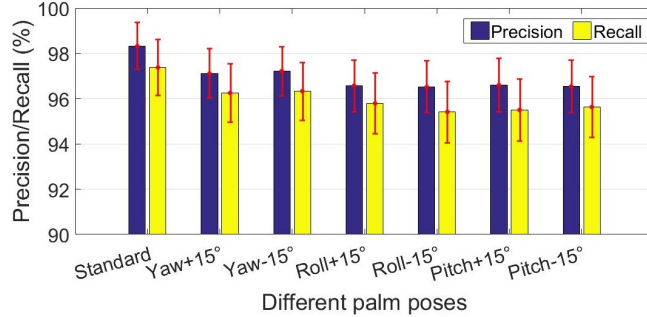


Figure 12. Different palm poses analysis.

Besides, to continue comparing the performances with different distance metrics, we employed the McNemar's test [18], a frequently used test for authentication application. The null hypothesis is that these distance metrics have equal performances. If *p-value* is less than  $\alpha$  (0.05 in this test), it rejects the hypothesis and concludes that *EMD-VT* has superior performance over others. Then the test results show all *p-values* stay below 0.05. *P-values* with Euclidean and Hamming are both around 0.01 and with Hausdorff it is around 0.02. This indicates strong evidence to reject the null hypothesis and *EMD-VT* outperforms others.

**7.4.2 Palm Robustness Analysis.** In daily-life applications, the sensing environment is not always ideal. Also users might put their hands in different poses, not right above in a standard way when authentication. The same person with different poses or hand positions leads to different PA field interferences and different PA sensing results. For the robustness and usability test, in this section, we conduct several experiments to investigate those effects on our *PAvesse* system.

**Different Palm Poses:** We evaluate the system performance with different palm poses. We scan the users' palm veins in seven ways following the Experimental Procedure: (i) standard, (ii) yaw clockwise by 15 degrees (+15°), (iii) yaw counter-clockwise by 15 degrees (−15°), (iv) roll clockwise by 15 degrees, (v) roll counter-clockwise by 15 degrees, (vi) pitch clockwise by 15 degrees, (vii) pitch counter-clockwise by 15 degrees. Other steps are the same in the Data Partition. Finally, we repeat experiments 10 times and calculate the average performance.

The data in Figure 12 show the results of testing with these seven different hand poses. In all cases, the precision and recall are all higher than 95% and the variations are all lower than 1.4%. The precision and recall achieve the highest value under a standard pose, 98.33% and 97.37% respectively. The variations are 1.04% and 1.24% correspondingly. These results demonstrates that the system performs effectively for distinct hand poses, offering excellent usability. In addition, this strong and flexible operation is generally comparable to other user-friendly means of authentication, like the fingerprint. For roll and pitch poses, the performance goes down 1.8% from the highest value. Considering the laser source is vertical from top to bottom, we notice that the effective ROI in these poses is reduced and the palm vein structure has a little deformation due to the different laser incident angles. This increases the difficulty of feature matching, which weakens the final performance and decreases the precision; while ROI and palm veins are less affected in yaw poses.

Table 4. The execution time for different palm poses.

Poses	Average time (s)
Standard	1.13
Yaw +15°	1.42
Yaw -15°	1.46
Roll +15°	1.72
Roll -15°	1.74
Pitch +15°	1.75
Pitch -15°	1.79

The average execution time for each pose is calculated and described in Table 4. All poses cost less than 2s. For the standard pose, the execution time is 1.13s. For yaw poses, the execution time is around 1.44s. For roll poses, it is about 1.73s and for pitch poses, it is about 1.77s. With the development of CPU and GPU, the execution time would be reduced much further.

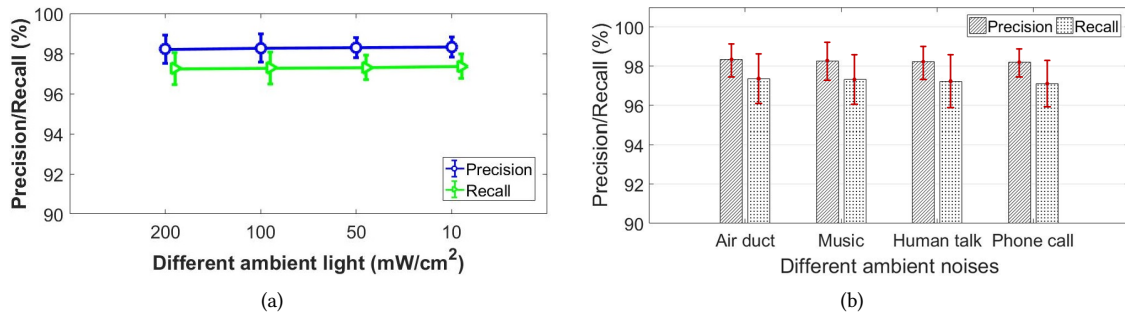


Fig. 13. (a) records ambient noise analysis effect on the system. (b) records ambient noise analysis on the system.

**Environmental Sensitivity Analysis:** In practical application, there are many variables in the environment. Ambient noise and light are always the most common issues in the sensing field, especially in the biometrics scenarios. In this experiment, we investigate these two effects on our *PA vessel* system. It is very helpful to change the light to fulfill different application requirements. We identify the light by the radiation intensity of illumination. We set different levels of visible light strength,  $10mW/cm^2$ ,  $50mW/cm^2$ ,  $100mW/cm^2$  and  $200mW/cm^2$ , for the experiment environment. Next, we employ 4 common types of sound in daily life as ambient noise, air duct, music, human talk and phone call. All of them keep at 50db. Under each effect, we follow the step in the Experimental Procedure and the Data Partition and repeat the experiment 10 times for each test. Then we apply our system to evaluate its precision and recall. The authentication performance of this palm vein is shown in the following.

**Ambient Light:** Figure 13(a) demonstrates that the precision and recall are both higher than 97% and the variations are all less than 2%. The performance would not weaken along the illumination intensity. This conforms to the theory. The laser in our system has a 10 Hz pulse repetition rate. Only when the light source has a similar pulse rate, it can excite the palm to emit ultrasound, thereby affecting the ultrasound emission or detection. While in ordinary scenarios, general lighting does not have such a characteristic.

**Ambient Noise:** Figure 13(b) illustrates that precision and recall are not affected by four ambient noise scenarios. They are the same as the standard in relaxed status, which also accords with the mechanism. Moreover, the variations are constant. Our detector has an operation wavelength, within the ultrasound range, around a certain center frequency at the nanometer level to avoid the impact of ambient noises on our system's performance.

## 8 DISCUSSION

### 8.1 PA Sensing System Optimization

**Portability:** Till date, the diode-pumped laser sources and LEDs have shown the potential for reducing the system size, while numerous studies continue to explore its usage for power consumption. The decisive PA sensing device can be integrated within a  $50cm \times 50cm$  optical breadboard with a compact high power flashlamp-pumped laser (if available). The lasers are generally preferred since the power output of existing LEDs is inadequate and requires significant amplification and averaging. There is an abundant amount of research in this field, and these sources are being constantly improved. Once these constraints have been addressed, then the LEDs can be incorporated into our system, which would immensely improve the system's mobility. Besides, diode lasers or

LEDs can perform at a higher pulse repetition rate (1 kHz vs. 10 Hz in our current laser), which will reduce the imaging time to sub-second.

**Commodity Exploration:** We perform an experiment to explore the effect of transducer type on the resolution. We utilize an economical and widely accessible 5MHz clinical ultrasound transducer array with 128 elements designed for deep-tissue imaging at over 5cm depth. In comparison with the proposed IR camera setup, the resolution increases to approximately four times. The resolution can be further improved by employing higher frequency transducers. For instance, the deployment of 15MHz transducer array enhances the spatial resolution by three times, *i.e.*, around 100microns, relative to our current setup. However, the transducer element size decreases with increase in frequency, as each element is of the size of one acoustic wavelength. Moreover, a rise in frequency exponentially raises the fabrication cost and complexity. For palm imaging, we can achieve commercial standards with the clinical transducer itself.

## 8.2 PA Sensing for Future Medical and Healthcare Applications

**Nanomedicine:** The acquisition of sufficient pathological information is critical for disease-oriented diagnosis. The PA possess the capability to be a dynamic tool for nanomedicine as it can provide functional and structural sensing images with outstanding resolution and contrast [60, 94]. Although this field is still in its infancy, there is a bright outlook for emerging biomedical applications in nanomedicine.

**Drug Delivery:** Recent advancement in PA has lead researchers to explore its applications related to drug delivery, primarily concerning monitoring of either drugs or their effects [81]. Alternatively, PA can be used to directly govern the accumulation of various light-absorbing contrast agents or carriers with theranostic properties.

**Human-computer Interface:** As the technological dimension continues to integrate with every aspect of human life, it is vital to advance the domain of human-computer interface by researching innovative strategies and techniques. Existing evolution of neurotechnologies makes a great effort to address these issues through novel concepts that directly link biological activity to computers, which naturally matches with PA [24]. Besides, considering the PA short response time for the biological signal (within 1ms), PA would have a bright future in this domain.

## 9 CONCLUSION

In this paper, we propose *PA vessel*, a reliable and robust 3D photoacoustic vessel structure sensing system which is able to capture the high-resolution 3D vessel structure traits of individuals. The entire system comprises two key components, PA sensing hardware and PA sensing software. Specifically, we design and implement the hardware prototype based on the PA concept. We develop the advanced image reconstruction and 3D photoacoustic vein model to reconstruct the 3D vessel structure from the received ultrasound signal. The results in the evaluation confirm the excellent sensing performance of *PA vessel*. In the end, a case study of PA biometric applications is conducted. Based on the physiological properties of the human palm, we develop a new 3D vascular matching algorithm *EMD-VT* to effectively differentiate the vessel structure among individuals. The intensive experiments demonstrate the effectiveness, reliability and robustness of our proposed system in biometrics.

## ACKNOWLEDGMENTS

We thank all anonymous reviewers for their insightful comments on this paper. This work was in part supported by the National Science Foundation under grant No.1564104 and No.1718375.

## REFERENCES

- [1] Dorit D Adler, Paul L Carson, Jonathan M Rubin, and Dana Quinn-Reid. 1990. Doppler ultrasound color flow imaging in the study of breast cancer: preliminary findings. *Ultrasound in medicine & biology* 16, 6 (1990), 553–559.

- [2] Md Zahangir Alom, Moin Mostakim, Rubel Biswas, and Amitabha Chakrabarty. 2014. Automatic Slice Growing Method based 3D reconstruction of liver with its vessels. In *Computer and Information Technology (ICCIT), 2013 16th International Conference on*. IEEE, 338–344.
- [3] Vassilis Athitsos and Stan Sclaroff. 2002. An appearance-based framework for 3D hand shape classification and camera viewpoint estimation. In *Automatic Face and Gesture Recognition, 2002. Proceedings. Fifth IEEE International Conference on*. IEEE, 45–50.
- [4] SF Bahgat, S Ghoniemy, and M Alotaibi. 2013. Proposed multimodal palm veins-face biometric authentication. *International journal of advanced computer science and applications* 4, 6 (2013), 92–96.
- [5] Asim Baig, Ahmed Bouridane, Fatih Kurugollu, and Gang Qu. 2009. Fingerprint-Iris fusion based identification system using a single hamming distance matcher. In *Bio-inspired Learning and Intelligent Systems for Security, 2009. BLISS'09. Symposium on*. IEEE, 9–12.
- [6] Paul Beard. 2011. Biomedical photoacoustic imaging. *Interface focus* (2011), rsfs20110028.
- [7] Paul C Beard and Timothy N Mills. 2001. 2D line-scan photoacoustic imaging of absorbers in a scattering tissue phantom. In *Biomedical Optoacoustics II*, Vol. 4256. International Society for Optics and Photonics, 34–43.
- [8] Alexander Graham Bell. 1880. Upon the production and reproduction of sound by light. *Journal of the Society of Telegraph Engineers* 9, 34 (1880), 404–426.
- [9] Lacey Best-Rowden and Anil K Jain. 2018. Longitudinal study of automatic face recognition. *IEEE transactions on pattern analysis and machine intelligence* 40, 1 (2018), 148–162.
- [10] Rachel Bitton, Roger Zemp, Jesse Yen, Lihong V Wang, and K Kirk Shung. 2009. A 3-D high-frequency array based 16 channel photoacoustic microscopy system for in vivo micro-vascular imaging. *IEEE transactions on medical imaging* 28, 8 (2009), 1190–1197.
- [11] A Cedola, A Bravin, I Bukreeva, M Fratini, A Pacureanu, A Mittone, L Massimi, P Cloetens, P Coan, G Campi, et al. 2017. X-Ray Phase Contrast Tomography Reveals Early Vascular Alterations and Neuronal Loss in a Multiple Sclerosis Model. *Scientific Reports* 7, 1 (2017), 5890.
- [12] Sung-Liang Chen, Tao Ling, Sheng-Wen Huang, Hyoung Won Baac, and L Jay Guo. 2010. Photoacoustic correlation spectroscopy and its application to low-speed flow measurement. *Optics letters* 35, 8 (2010), 1200–1202.
- [13] Liang Cheng, Jingjing Liu, Xing Gu, Hua Gong, Xiaoze Shi, Teng Liu, Chao Wang, Xiaoyong Wang, Gang Liu, Huaiyong Xing, et al. 2014. PEGylated WS2 nanosheets as a multifunctional theranostic agent for in vivo dual-modal CT/photoacoustic imaging guided photothermal therapy. *Advanced materials* 26, 12 (2014), 1886–1893.
- [14] National Research Council et al. 2004. *Existing and potential standoff explosives detection techniques*. National Academies Press.
- [15] Marc Dewey and Marc Kachelrieß. 2018. Fundamentals of X-Ray Computed Tomography: Acquisition and Reconstruction. In *Quantification of Biophysical Parameters in Medical Imaging*. Springer, 325–339.
- [16] O Dóka, D Bicanic, and R Frankhuizen. 1999. Photoacoustic study of heated binary mixtures containing whey and skimmed-milk powders. *Zeitschrift für Lebensmitteluntersuchung und-Forschung A* 208, 1 (1999), 1–5.
- [17] Ottó Dóka, József Kispéter, and András Lőrincz. 1991. Potential value of photoacoustic spectroscopy for determining iron content of milk protein concentrates. *Journal of dairy research* 58, 4 (1991), 453–460.
- [18] Morten W Fagerland, Stian Lydersen, and Petter Laake. 2013. The McNemar test for binary matched-pairs data: mid-p and asymptotic are better than exact conditional. *BMC medical research methodology* 13, 1 (2013), 91.
- [19] Christopher P Favazza, Lihong V Wang, and Lynn A Cornelius. 2011. In vivo functional photoacoustic microscopy of cutaneous microvasculature in human skin. *Journal of biomedical optics* 16, 2 (2011), 026004.
- [20] Richard Ribón Fletcher, Varsha Raghavan, Rujia Zha, Miriam Haverkamp, and Patricia L Hibberd. 2014. Development of mobile-based hand vein biometrics for global health patient identification. In *Global Humanitarian Technology Conference (GHTC), 2014 IEEE*. IEEE, 541–547.
- [21] Muhammad Moazam Fraz, Sarah A Barman, Paolo Remagnino, Andreas Hoppe, Abdul Basit, Bunyarit Uyyanonvara, Alicja R Rudnicka, and Christopher G Owen. 2012. An approach to localize the retinal blood vessels using bit planes and centerline detection. *Computer methods and programs in biomedicine* 108, 2 (2012), 600–616.
- [22] Deepa Gupta, Xing Chen, Chen-Chia Wang, Sudhir Trivedi, and Fow-Sen Choa. 2018. Stand-Off Chemical Detection Using Photoacoustic Sensing Techniques From Single Element to Phase Array. *Chemosensors* 6, 1 (2018), 6.
- [23] Puneet Gupta, Saurabh Srivastava, and Phalguni Gupta. 2016. An accurate infrared hand geometry and vein pattern based authentication system. *Knowledge-Based Systems* 103 (2016), 143–155.
- [24] Bin He, Todd Coleman, Guy M Genin, Gary Glover, Xiaoping Hu, Nessa Johnson, Tianming Liu, Scott Makeig, Paul Sajda, and Kaiming Ye. 2013. Grand challenges in mapping the human brain: NSF workshop report. *IEEE transactions on Biomedical engineering* 60, 11 (2013), 2983–2992.
- [25] Audun Hordvik and H Schlossberg. 1977. Photoacoustic technique for determining optical absorption coefficients in solids. *Applied optics* 16, 1 (1977), 101–107.
- [26] Song Hu, Konstantin I Maslov, Vassiliy Tsytarev, and Lihong V Wang. 2009. Functional transcranial brain imaging by optical-resolution photoacoustic microscopy. *Journal of biomedical optics* 14, 4 (2009), 040503.

- [27] Peng Huang, Pengfei Rong, Jing Lin, Wanwan Li, Xuefeng Yan, Molly Gu Zhang, Liming Nie, Gang Niu, Jie Lu, Wei Wang, et al. 2014. Triphase interface synthesis of plasmonic gold bellflowers as near-infrared light mediated acoustic and thermal theranostics. *Journal of the American Chemical Society* 136, 23 (2014), 8307–8313.
- [28] Sang-Kyun Im, Hyung-Man Park, Soo-Won Kim, Chang-Kyung Chung, and Hwan-Soo Choi. 2000. Improved vein pattern extracting algorithm and its implementation. In *Consumer Electronics, 2000. ICCE. 2000 Digest of Technical Papers. International Conference on. IEEE*, 2–3.
- [29] Sang-Kyun Im, Hyung-Man Park, Young-Woo Kim, Sang-Chan Han, Soo-Won Kim, Chul-Hee Kang, and Chang-Kyung Chung. 2001. An biometric identification system by extracting hand vein patterns. *Journal-Korean Physical Society* 38, 3 (2001), 268–272.
- [30] Antonio Iula, Alessandro Savoia, and Giosuà Caliano. 2012. 3D Ultrasound palm vein pattern for biometric recognition. In *Ultrasonics Symposium (IUS), 2012 IEEE International. IEEE*, 1–4.
- [31] Anil K Jain, Sunpreet S Arora, Kai Cao, Lacey Best-Rowden, and Anjoo Bhatnagar. 2017. Fingerprint Recognition of Young Children. *IEEE Transactions on Information Forensics and Security* 12, 7 (2017), 1501–1514.
- [32] Shuliang Jiao, Minshan Jiang, Jianming Hu, Amani Fawzi, Qifa Zhou, K Kirk Shung, Carmen A Puliafito, and Hao F Zhang. 2010. Photoacoustic ophthalmoscopy for in vivo retinal imaging. *Optics express* 18, 4 (2010), 3967–3972.
- [33] Elizabeth AV Jones, Ferdinand le Noble, and Anne Eichmann. 2006. What determines blood vessel structure? Genetic prespecification vs. hemodynamics. *Physiology* 21, 6 (2006), 388–395.
- [34] Chulhong Kim, Todd N Erpelding, Konstantin I Maslov, Ladislav Jankovic, Walter J Akers, Liang Song, Samuel Achilefu, Julie A Margenthaler, Michael D Pashley, and Lihong V Wang. 2010. Handheld array-based photoacoustic probe for guiding needle biopsy of sentinel lymph nodes. *Journal of biomedical optics* 15, 4 (2010), 046010.
- [35] Seyed Mehdi Lajevardi, Arathi Arakala, Stephen Davis, and Kathy J Horadam. 2014. Hand vein authentication using biometric graph matching. *IET Biometrics* 3, 4 (2014), 302–313.
- [36] Mikael Lassen, David Balslev-Harder, Anders Brusich, Nikola Pelevic, Stefan Persijn, and Jan C Petersen. 2018. Design and experimental verification of a photoacoustic flow sensor using computational fluid dynamics. *Applied optics* 57, 4 (2018), 802–806.
- [37] Eui Chul Lee and Kang Ryoung Park. 2011. Image restoration of skin scattering and optical blurring for finger vein recognition. *Optics and Lasers in Engineering* 49, 7 (2011), 816–828.
- [38] Jen-Chun Lee. 2012. A novel biometric system based on palm vein image. *Pattern Recognition Letters* 33, 12 (2012), 1520–1528.
- [39] Ming-Yih Lee and Chi-Shih Yang. 2010. Entropy-based feature extraction and decision tree induction for breast cancer diagnosis with standardized thermograph images. *Computer methods and programs in biomedicine* 100, 3 (2010), 269–282.
- [40] Fang Li, Maylor KH Leung, and Xiaozhou Yu. 2004. Palmprint identification using Hausdorff distance. In *Biomedical Circuits and Systems, 2004 IEEE International Workshop on. IEEE*, S3–3.
- [41] Chih-Lung Lin and Kuo-Chin Fan. 2004. Biometric verification using thermal images of palm-dorsa vein patterns. *IEEE Transactions on Circuits and Systems for Video Technology* 14, 2 (2004), 199–213.
- [42] Feng Lin, Kun Woo Cho, Chen Song, Wenyao Xu, and Zhanpeng Jin. 2018. Brain Password: A Secure and Truly Cancelable Brain Biometrics for Smart Headwear. In *Proceedings of the 16th Annual International Conference on Mobile Systems, Applications, and Services. ACM*, 296–309.
- [43] Feng Lin, Chen Song, Yan Zhuang, Wenyao Xu, Changzhi Li, and Kui Ren. 2017. Cardiac Scan: A Non-contact and Continuous Heart-based User Authentication System. In *Proceedings of the 23rd Annual International Conference on Mobile Computing and Networking. ACM*, 315–328.
- [44] Wei Liu, Bangxin Lan, Leo Hu, Ruimin Chen, Qifa Zhou, and Junjie Yao. 2017. Photoacoustic thermal flowmetry with a single light source. *Journal of biomedical optics* 22, 9 (2017), 096001.
- [45] Jordan S Lum, David M Stobbe, Mark A Borden, and Todd W Murray. 2018. Photoacoustic technique to measure temperature effects on microbubble viscoelastic properties. *Applied physics letters* 112, 11 (2018), 111905.
- [46] Martin Magnusson, Achim Lilienthal, and Tom Duckett. 2007. Scan registration for autonomous mining vehicles using 3D-NDT. *Journal of Field Robotics* 24, 10 (2007), 803–827.
- [47] Richard Martel, Christophe N N’Soukpoe-Kossi, Paul Paquin, and Roger M Leblanc. 1987. Photoacoustic analysis of some milk products in ultraviolet and visible light. *Journal of dairy science* 70, 9 (1987), 1822–1827.
- [48] Konstantin Maslov, Hao F Zhang, Song Hu, and Lihong V Wang. 2008. Optical-resolution photoacoustic microscopy for in vivo imaging of single capillaries. *Optics letters* 33, 9 (2008), 929–931.
- [49] Goh Kah Ong Michael, Tee Connie, Teo Chuan Chin, Neo Han Foon, and Andrew Teoh Beng Jin. 2010. Realizing hand-based biometrics based on visible and infrared imagery. In *International Conference on Neural Information Processing. Springer*, 606–615.
- [50] Noboru Niki, Yoshiki Kawata, Hitoshi Satoh, and Tatsuo Kumazaki. 1993. 3D imaging of blood vessels using x-ray rotational angiographic system. In *Nuclear Science Symposium and Medical Imaging Conference, 1993., 1993 IEEE Conference Record. IEEE*, 1873–1877.
- [51] James F O’Brien and Norberto F Ezquerro. 1994. *Automated segmentation of coronary vessels in angiographic image sequences utilizing temporal, spatial and structural constraints*. Technical Report. Georgia Institute of Technology.

- [52] CKN Patel. 2008. Laser photoacoustic spectroscopy helps fight terrorism: High sensitivity detection of chemical warfare agent and explosives. *The European Physical Journal Special Topics* 153, 1 (2008), 1–18.
- [53] Manojit Pramanik and Lihong V Wang. 2009. Thermoacoustic and photoacoustic sensing of temperature. *Journal of biomedical optics* 14, 5 (2009), 054024.
- [54] Tauhidur Rahman, Alexander Travis Adams, Perry Schein, Aadhar Jain, David Erickson, and Tanzeem Choudhury. 2016. Nutrilizer: A Mobile System for Characterizing Liquid Food with Photoacoustic Effect. In *SenSys*. 123–136.
- [55] Zhou Ren, Junsong Yuan, and Zhengyou Zhang. 2011. Robust hand gesture recognition based on finger-earth mover’s distance with a commodity depth camera. In *Proceedings of the 19th ACM international conference on Multimedia*. ACM, 1093–1096.
- [56] Arun Ross, Anil Jain, and S Pankati. 1999. A prototype hand geometry-based verification system. In *Proceedings of 2nd conference on audio and video based biometric person authentication*. 166–171.
- [57] Guy Rousseau, Alain Blouin, and Jean-Pierre Monchalain. 2012. Non-contact photoacoustic tomography and ultrasonography for tissue imaging. *Biomedical optics express* 3, 1 (2012), 16–25.
- [58] Kathryn J Rowland, Junjie Yao, Lidai Wang, Christopher R Erwin, Konstantin I Maslov, Lihong V Wang, and Brad W Warner. 2012. Immediate alterations in intestinal oxygen saturation and blood flow after massive small bowel resection as measured by photoacoustic microscopy. *Journal of pediatric surgery* 47, 6 (2012), 1143–1149.
- [59] Yossi Rubner and Carlo Tomasi. 2001. The earth mover’s distance. In *Perceptual Metrics for Image Database Navigation*. Springer, 13–28.
- [60] Pratik Samant, Armando Hernandez, Shelby Conklin, and Liangzhong Xiang. 2017. Nanoscale Photoacoustic Tomography (nPAT) for label-free super-resolution 3D imaging of red blood cells. In *Nanoimaging and Nanospectroscopy V*, Vol. 10350. International Society for Optics and Photonics, 103500P.
- [61] Raul Sanchez-Reillo, Carmen Sanchez-Avila, and Ana Gonzalez-Marcos. 2000. Biometric identification through hand geometry measurements. *IEEE Transactions on pattern analysis and machine intelligence* 22, 10 (2000), 1168–1171.
- [62] Alok Sarwal and AP Dhawan. 1994. 3-d reconstruction of coronary arteries. In *Engineering in Medicine and Biology Society, 1994. Engineering Advances: New Opportunities for Biomedical Engineers. Proceedings of the 16th Annual International Conference of the IEEE*, Vol. 1. IEEE, 504–505.
- [63] HP Schwan. 1994. Engineering in Medicine and Biology Society, 1994. Engineering Advances: New Opportunities for Biomedical Engineers. Proceedings of the 16th Annual International Conference of the IEEE. (1994).
- [64] Sanasam Sunderlal Singh, Prahlad Kr Baruah, Alike Khare, and Shrikrishna N Joshi. 2018. Effect of laser beam conditioning on fabrication of clean micro-channel on stainless steel 316L using second harmonic of Q-switched Nd: YAG laser. *Optics & Laser Technology* 99 (2018), 107–117.
- [65] Yunpeng Song, Zhongmin Cai, and Zhi-Li Zhang. 2017. Multi-touch Authentication Using Hand Geometry and Behavioral Information. In *Security and Privacy (SP), 2017 IEEE Symposium on*. IEEE, 357–372.
- [66] Jacob Staley, Patrick Grogan, Abbas K Samadi, Huihong Cui, Mark S Cohen, and Xinmai Yang. 2010. Growth of melanoma brain tumors monitored by photoacoustic microscopy. *Journal of biomedical optics* 15, 4 (2010), 040510.
- [67] Fedor V Subach, Lijuan Zhang, Theodoros WJ Gadella, Nadya G Gurskaya, Konstantin A Lukyanov, and Vladislav V Verkhusha. 2010. Red fluorescent protein with reversibly photoswitchable absorbance for photochromic FRET. *Chemistry & biology* 17, 7 (2010), 745–755.
- [68] Yuki Sugano, Shinya Onogi, Antoine Bossard, Takashi Mochizuki, and Kohji Masuda. 2012. Development of a 3D reconstruction of blood vessel by positional calibration of ultrasound probe. In *Biomedical Engineering International Conference (BMEiCON), 2012*. IEEE, 1–4.
- [69] Takamsa Tamura, Sayaka Matsuda, Seira Shigekuni, Risaco Tanaka, Chihiro Tsutsui, and Takamichi Hirata. 2017. Direct Near Infrared Imaging of Brain Surface Blood Vessel Using Indocyanine Green Angiography. *Bulletin of the American Physical Society* 62 (2017).
- [70] Adrian Taruttis, Eva Herzog, Daniel Razansky, and Vasilis Ntziachristos. 2010. Real-time imaging of cardiovascular dynamics and circulating gold nanorods with multispectral photoacoustic tomography. *Optics express* 18, 19 (2010), 19592–19602.
- [71] K Trieb. 2016. The Charcot foot: pathophysiology, diagnosis and classification. *Bone Joint J* 98, 9 (2016), 1155–1159.
- [72] Corinne Veyrac, Catherine Baud, Christophe Lopez, Alain Couture, Magali Saguintaah, and Michel Averous. 2003. The value of colour Doppler ultrasonography for identification of crossing vessels in children with pelvi-ureteric junction obstruction. *Pediatric radiology* 33, 11 (2003), 745–751.
- [73] Aosen Wang, Tianjiao Wang, Chi Zhou, and Wenyao Xu. 2017. LuBan: Low-Cost and In-Situ Droplet Micro-Sensing for Inkjet 3D Printing Quality Assurance. In *Proceedings of the 15th ACM Conference on Embedded Network Sensor Systems*. ACM, 27.
- [74] Lihong V Wang. 2008. Prospects of photoacoustic tomography. *Medical physics* 35, 12 (2008), 5758–5767.
- [75] Lihong V Wang. 2010. Photoacoustic tomography. In *Optical-Thermal Response of Laser-Irradiated Tissue*. Springer, 743–760.
- [76] Lihong V Wang and Song Hu. 2012. Photoacoustic tomography: in vivo imaging from organelles to organs. *Science* 335, 6075 (2012), 1458–1462.
- [77] Xueding Wang, Geng Ku, Malgorzata A Wegiel, Darryl J Bornhop, George Stoica, and Lihong V Wang. 2004. Noninvasive photoacoustic angiography of animal brains in vivo with near-infrared light and an optical contrast agent. *Optics letters* 29, 7 (2004), 730–732.
- [78] Grover C Wetsel. 1980. Photoacoustic effect in piezoelectric ceramics. *JOSA* 70, 5 (1980), 471–474.

- [79] MCY Wong, G Piaggio, MB Damasio, C Molinelli, SM Ferretti, A Pistorio, G Ghiggeri, ML Degl'Innocenti, A Canepa, V Incarbone, et al. 2017. Hydronephrosis and crossing vessels in children: Optimization of diagnostic-therapeutic pathway and analysis of color Doppler ultrasound and magnetic resonance urography diagnostic accuracy. *Journal of pediatric urology* (2017).
- [80] Hongpeng Wu, Lei Dong, Huadan Zheng, Yajun Yu, Weiguang Ma, Lei Zhang, Wangbao Yin, Liantuan Xiao, Suotang Jia, and Frank K Tittel. 2017. Beat frequency quartz-enhanced photoacoustic spectroscopy for fast and calibration-free continuous trace-gas monitoring. *Nature communications* 8 (2017), 15331.
- [81] Jun Xia, Chulhong Kim, and Jonathan F Lovell. 2015. Opportunities for photoacoustic-guided drug delivery. *Current drug targets* 16, 6 (2015), 571–581.
- [82] Jun Xia and Lihong V Wang. 2014. Small-animal whole-body photoacoustic tomography: a review. *IEEE Transactions on Biomedical Engineering* 61, 5 (2014), 1380–1389.
- [83] Jun Xia, Junjie Yao, and Lihong V Wang. 2014. Photoacoustic tomography: principles and advances. *Electromagnetic waves (Cambridge, Mass.)* 147 (2014), 1.
- [84] Minghua Xu and Lihong V Wang. 2005. Universal back-projection algorithm for photoacoustic computed tomography. *Physical Review E* 71, 1 (2005), 016706.
- [85] Minghua Xu and Lihong V Wang. 2006. Photoacoustic imaging in biomedicine. *Review of scientific instruments* 77, 4 (2006), 041101.
- [86] Zhisheng Yan, Chen Song, Feng Lin, and Wenyao Xu. 2018. Exploring Eye Adaptation in Head-Mounted Display for Energy Efficient Smartphone Virtual Reality (*HotMobile'18*). 13–18.
- [87] Junjie Yao, Konstantin I Maslov, Ernest R Puckett, Kathryn J Rowland, Brad W Warner, and Lihong V Wang. 2012. Double-illumination photoacoustic microscopy. *Optics letters* 37, 4 (2012), 659–661.
- [88] Junjie Yao, Jun Xia, Konstantin I Maslov, Mohammadreza Nasiriavanaki, Vassiliy Tsytsarev, Alexei V Demchenko, and Lihong V Wang. 2013. Noninvasive photoacoustic computed tomography of mouse brain metabolism in vivo. *Neuroimage* 64 (2013), 257–266.
- [89] Chun Yuan, Eugene Lin, Jacob Millard, and Jenq-Neng Hwang. 1999. Closed contour edge detection of blood vessel lumen and outer wall boundaries in black-blood MR images. *Magnetic resonance imaging* 17, 2 (1999), 257–266.
- [90] RJ Zemp, L Song, R Bitton, KK Shung, and LV Wang. 2008. Realtime photoacoustic microscopy of murine cardiovascular dynamics. *Optics express* 16, 22 (2008), 18551–18556.
- [91] Hao F Zhang, Konstantin Maslov, Meng-Lin Li, George Stoica, and Lihong V Wang. 2006. In vivo volumetric imaging of subcutaneous microvasculature by photoacoustic microscopy. *Optics Express* 14, 20 (2006), 9317–9323.
- [92] Huai Geng Zheng. 2017. *Static and dynamic analysis of near infra-red dorsal hand vein images for biometric applications*. Ph.D. Dissertation. University of Central Lancashire.
- [93] Xia Zhu, Xiaoming Hu, Dayuan Yan, Ya Zhou, Ruobing Huang, and Meiqing Liu. 2013. A 3D interpolation method in repairing hand vascular tree for vein recognition. In *Imaging Systems and Techniques (IST), 2013 IEEE International Conference on*. IEEE, 254–258.
- [94] Chunpeng Zou, Beibei Wu, Yanyan Dong, Zhangwei Song, Yaping Zhao, Xianwei Ni, Yan Yang, and Zhe Liu. 2017. Biomedical photoacoustics: fundamentals, instrumentation and perspectives on nanomedicine. *International journal of nanomedicine* 12 (2017), 179.

Received November 2017; revised May 2018; accepted September 2018